Development of Grating for the Optical Addressing of Sr^+ Ions With Data Analysis Techniques

Yu Dian Lim, *Member, IEEE*, Peng Zhao, *Member, IEEE*, Luca Guidoni, Jean-Pierre Likforman, and Chuan Seng Tan, *Fellow, IEEE*

***Abstract*—In this study, SiN-based gratings with various radius of curvature (*r*) are designed and fabricated for the optical addressing of trapped Sr^+ ion. The beam width of the light coupled out from the gratings is investigated using a self-developed Python-based data analysis technique. It is found that the *r* values have insignificant influence on the beam width along *x*-axis; whereas the beam waist along *y*-axis reduces from 13.96 to 12.3 μm as *r* increases from 15 to 20 μm, then increases gradually to 20.51 μm as the *r* value further increases to 60 μm. The obtained results can provide a versatile solution on the optical addressing of trapped Sr^+ for applications in quantum engineering.**

***Index Terms*—Arrayed waveguide gratings, optical beams, python, qubit, silicon photonics.**

I. Introduction

OPTICAL addressing is a crucial part in the realization of quantum devices with trapped ions, such as quantum computer and quantum clock [1], [2]. In quantum operations, trapped ion qubits require optical addressing from laser light of specific wavelengths for various operations, including ion cooling, <1> to <0> state shifting, clearing out energy level, etc. To minimize the form factor of chip-based ion trap devices, silicon photonics (SiPh) integration has been widely developed [3].

In the field of SiPh-integrated ion trap devices, Lincoln Laboratory exhibited a chip-based surface-electrode ion-trap that with integrated waveguides and grating couplers to provide the all wavelengths of light needed for the optical addressing of Sr^+ quantum bits [4]. Meanwhile, ETH Zurich used a scalable SiPh-integrated surface-electrode ion trap to achieve high-fidelity multi-ion quantum logic gates, with direct fibre coupling on multiple channels [5]. Recently, Sandia National Laboratory reported integration of SiPh components on surface ion trap, including waveguides, grating couplers, optical modulators, and single-photon avalanche detector (SPAD) for quantum devices, including quantum computer and quantum clock [6].

For precise optical addressing of trapped ion, the focusing of light beam coupled out from the grating structure is crucial. One of the well-established techniques include apodised grating structure which reported to show high efficiency of −3.10 dB [7]. However, apodised grating only focuses the light beam from the in-plane axis of the grating. Thus, in our previous work, we reported the investigation on the focusing of grating coupler with various radius of curvatures (r) on Silicon-On-Insulator (SOI) platform. Beam focusing along the out-of-plane axis has been observed [8]. However, the focusing was demonstrated on 1630 nm wavelength on silicon-on-insulator (SOI) platform, which is not applicable for optical addressing of trapped ions. At the same time, the determination of beam waist along x-axis (in-plane) and y-axis (out-of-plane) was carried out through manual measurement and one-by-one computational techniques. This hinders realization of fast, standardize analysis of multiple beam profiles, especially analyzing mass amount of beam profile data.

In this study, we explored the focusing of light beam coupled out from the grating coupler fabricated on Silicon Nitride (SiN) platform under 1092 nm wavelength laser light, which was widely used for the clear-out operation for the trapped Sr^+ ions quantum computers. It has been reported that SOI platform is suitable for silicon photonics at near- to mid-infrared (NIR and MIR) range, due to the high transmissivity of silicon for NIR to MIR light (∼1200 nm onwards) [9]. Thus, the SOI is selected for grating design under 1630 nm wavelength in our previous study [8]. In the case of 1092 nm, SiN platform is selected due to the high transmissivity of SiN for visible and NIR range, which covers the wavelength-of-interest in this study [10].

For automated, fast computation of beam waists, full-width half maximum (FWHM) and other crucial parameters, the obtained data is analyzed using Python-based data analysis technique. The obtained result can add significant technical values to the SiPh-integration of ion trap devices. At the same time, the Python-based data analytical techniques developed for the study can provide an automated computational solution to obtain the parameters needed from the obtained beam profiles.

Manuscript received 10 March 2023; revised 24 May 2023; accepted 26 May 2023. Date of publication 29 May 2023; date of current version 16 June 2023. This work was supported by ANR-NRF Joint Grant Call under Grant NRF2020-NRF-ANR073 HIT. *(Corresponding author: Chuan Seng Tan.)*

Yu Dian Lim is with the School of Electrical and Electronics Engineering, Nanyang Technological University, Singapore 639798 (e-mail: yudian.lim@ntu.edu.sg).

Peng Zhao and Chuan Seng Tan are with the School of Electrical and Electronics Engineering, Nanyang Technological University,, Singapore 639798, and also with the Institute of Microelectronics, Agency for Science, Technology and Research (A∗STAR), Singapore 117685 (e-mail: zhao0275@e.ntu.edu.sg; tancs@ntu.edu.sg).

Luca Guidoni and Jean-Pierre Likforman are with the Laboratoire Matériaux et Phénomènes Quantiques (MPQ), Université de Paris, F-75205 Paris, France (e-mail: luca.guidoni@univ-paris-diderot.fr; jean-pierre.likforman@univ-paris-diderot.fr).

Digital Object Identifier 10.1109/JPHOT.2023.3281134

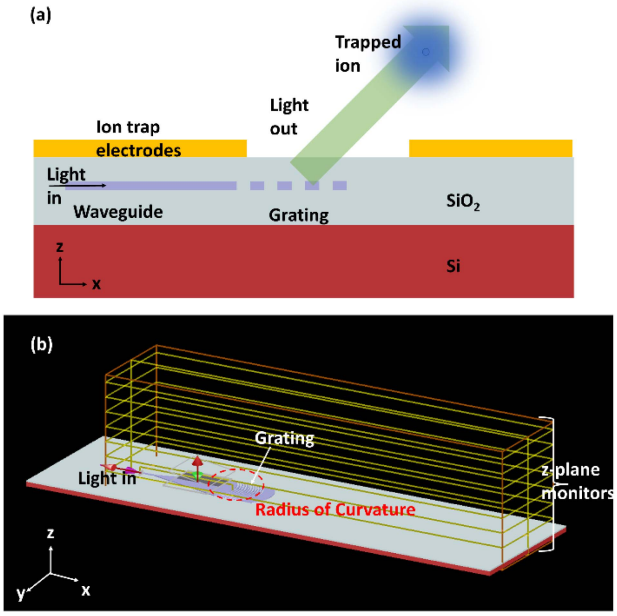

Fig. 1. (a) Illustration on the optical addressing of trapped ion with grating structure, (b) simulation model.

II. Design and Simulation

Fig. 1(a) illustrates the optical addressing of trapped ion with integrated grating coupler. As shown in the illustration, trapped ion requires planar electrodes with a combined RF/DC field to create a minimal pseudopotential point. The details of the ion-trapping mechanism are illustrate in ref. [11]. To investigate the effect of grating's radius of curvatures (r) on its corresponding beam waist, Finite-Difference Time-Domain (FDTD) simulation is carried out on gratings with various r, where the simulation model is shown in Fig. 1(b). Both y-plane monitor and z-plane monitors are included in the model, where z-plane monitors are placed at 10–70 μm above grating to investigate the light propagation along z-axis. 3-μm-thick top-oxide-layer (TOX) and buried-oxide-layer (BOX) is also included in the model. The material of the grating is SiN, where the pitch, duty cycle, SiN thickness, etch depth are fixed at 1.2 μm, 0.5, 0.4 μm, and 0.4 μm, respectively.

Fig. 2 shows the E-field distribution obtained from z-plane monitors in Fig. 1(b). The E-field data is first imported as DataFrames and plotted with Python. To investigate the changes in beam waist along z-axis for various r values, the beam waists along x- and y-axis at various heights are investigated. From Fig. 2, it is shown that the widths (along x- and y-axis) of the light beam focuses at 20 μm height, then increases gradually at increasing height. This shows the Gaussian properties in the propagation of light beam coupled out from the grating structure [3], [12], [13]. At the same time, the presence of multiple beams are observed along x-axis, due to the presence of multiple modes of the 1092 nm light coupled out from the grating structure [14], [15].

To determine the beam waists along x- and y-axis, linear lines parallel to x- and y-axis can be plotted on the light beams, where

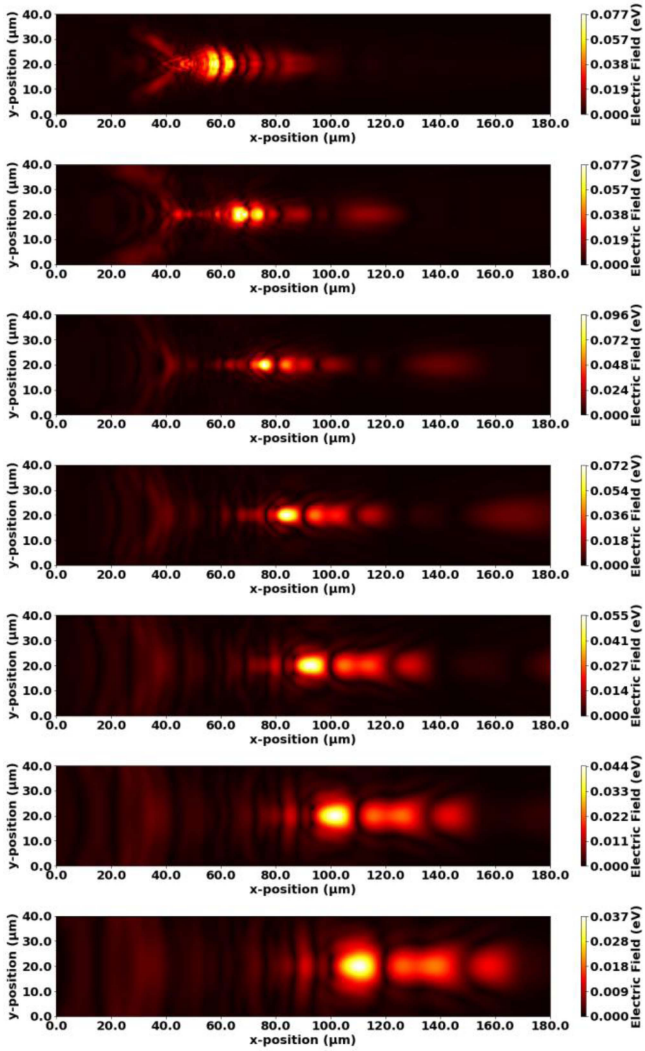

Fig. 2. E-field distribution in z-plane monitors from 10–70 μm ($r = 20$ μm).

the beam waists can be determined by finding the width of the plots. As the dimension of the z-plane monitors are fixed at 180 × 40 μm, the beam waist along x-axis is determined by plotting the E-field at y = 20 μm. For beam waist along y-axis, the beam waist is determined by searching the maximum value of the DataFrame used for E-field plotting, where the associated column of the maximum value is plotted as the E-field along y-axis. The abovementioned plots are shown in Fig. 3. As shown in Fig. 3(a) and (c), the peak electric fields reduce gradually at increasing heights. At the same time, multiple peaks present in every height, corresponding to the multiple modes present. These observations align with the E-field distribution plotted shown in Fig. 2. Comparing gratings with $r = 20$ and 60 μm, the beam waists along x-axis does not have significant changes across different values of r. On the contrary, the beam waist of $r = 20$ μm grating is significantly narrower than $r = 60$ μm.

To further investigate the beam waists of light coupled out from the corresponding gratings, the peak position, peak width, and FWHM of the beams across various r values and heights are computed using the scipy package in Python. The relevant

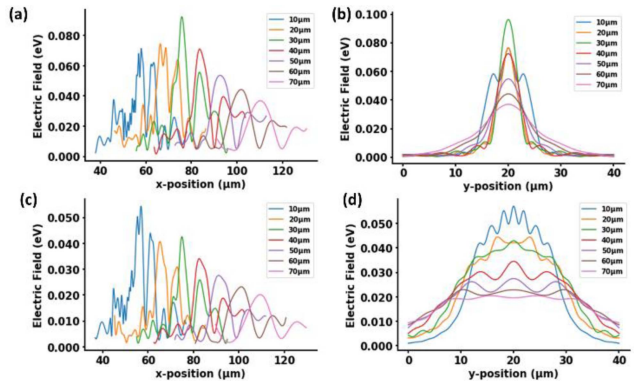

Fig. 3. E-field from grating with $r = 20$ um, (a) along x-axis, (b) along y = axis; E-field from grating with $r = 60$ um, (c) along x-axis, (d) along y = axis.

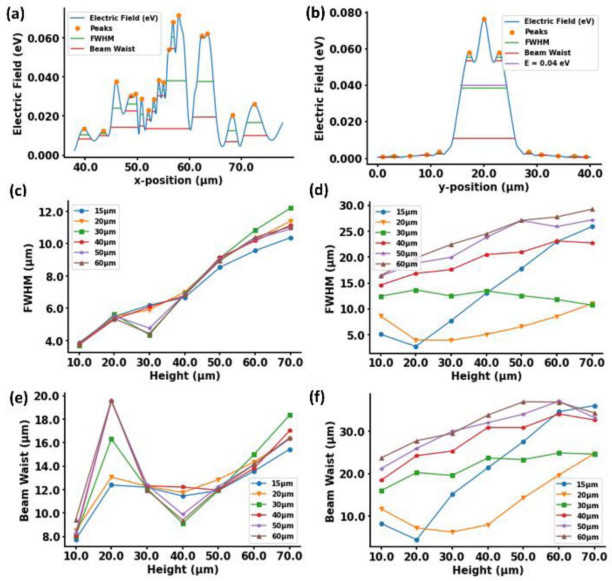

Fig. 4. E-field along (a) x-axis, (b) y-axis; FWHM along (c) x-axis, (d) y-axis; peak width at $1/e^2$ to the peak value along (e) x-axis, (f) y-axis.

Python code is given in ref. [16]. The FWHM is computed at 0.5 of the peaks; while the peak width is computed at 0.135, equivalent to $1/e^2$ of the peaks [17]. The typical plots of peak position, peak width, FWHM and E-field along x- and y-axis are shown in Fig. 5(a) and (b)(r = 30 μm grating at 10 μm height).

From Fig. 4(a), multiple peaks with corresponding FWHM and peak widths are found using scipy package in Python. This also in-line with the contour plot observed in Fig. 2, where multiple modes are observed along x-axis at various heights. Thus, only the peak width/FWHM with the highest corresponding peak values are taken and recorded. The peak widths and FWHM from grating with $r = 15$–60 μm at various heights, along x- and y-axis are shown in Fig. 4(c)–(f).

From Fig. 4(c) and (e), the beam waist and FWHM along x-axis do not correlate with the r values of the grating. This aligns with our previous study, where the x-axis width of the beam profiles from grating structure depends mainly on the pitch structure, including pitch size, duty cycle, etc. [8] From the

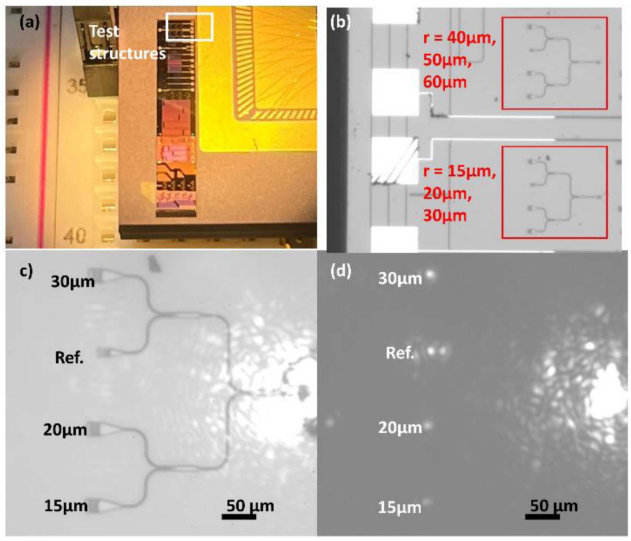

Fig. 5. (a) MPW die of this study, (b) test structures with $r = 15$ to 60 μm, (c) typical test structure of the gratings showing tested gratings and reference grating; (b) beams coupled out from the gratings viewed under CCD camera.

FWHM plot in Fig. 4(c), it can be observed that the beam waist along x-axis does not show significate changes with varying r values. Gratings with $r = 50$ and 60 μm focuses at 30 μm, which continues to propagate with beam waist similar to other investigated r values above 30 μm height. Similar observation was shown in Fig. 4(e). The beam waist from $r = 15$ to 60 μm at $1/e^2$ focuses at 40 μm height, then shows similar beam waist along x-axis at heights above 40 μm. This shows that the radius of curvature does not have significant impact on the beam waist along x-axis. For the varied FWHM in Fig. 4(c), this can be due to the varied peak position from different r values, which result in varied FWHM.

On the contrary, both beam waist and FWHM along y-axis changes with increasing r values of grating, as shown in Fig. 4(d) and (f). Generally, the FWHM and peak width of the beam coupled out from the grating increases along y-axis, except for $r = 15$ and 20 μm where the beam focuses at 20 and 30 μm heights. The beam waists along x-axis at the focal point of $r =$ 15 and 20 μm 4.41 and 6.23 μm, respectively. With r values from 30 to 60 μm, the beam waist along y-axis increases steadily from 15.12 to 29.46 μm. Similar trend was also observed in FWHM, where FWHM along y-axis focused from 9.42 to 5.16 μm as r increases from 15 to 20 μm, then increases steadily from 12.73 to 20.33 μm when r value increases further from 30 to 60 μm.

III. Experimental Details

Silicon Nitride (Si) gratings used in the simulations in Section II are fabricated from a multi-project wafer (MPW) scheme. The fabrication is carried out on 200 mm silicon wafer. First, 3 μm buried-oxide-layer (BOX) is deposited on the silicon surface, followed by 0.4 μm SiN. The SiN layer is then dry etched to form etch-through grating structures. 3 μm top-oxide-layer is then deposited on the grating structure. The obtained MPW die is shown in Fig. 5(a), where the location of

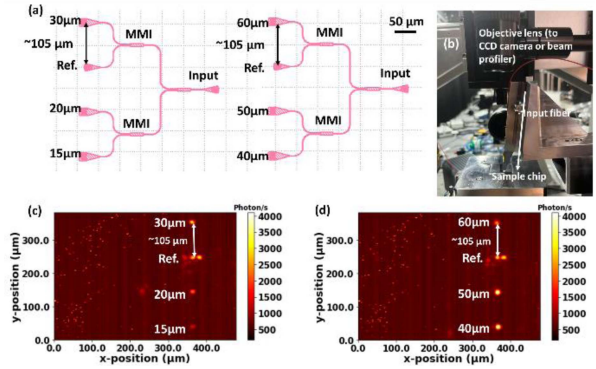

Fig. 6. (a) GDS design of the test structures, (b) measurement system for the beam profiles; beam profiles of: (b) $r = 15$, 20, and 30 μm; (c) $r = 40$, 50, and 60 μm under XC-130 ophir beam profiler.

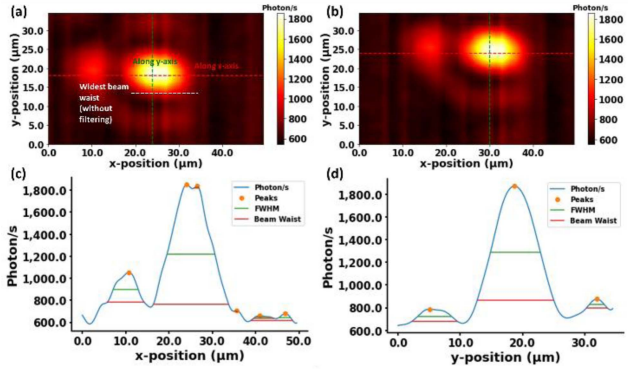

Fig. 7. Beam profile of light coupled out from $r = 30$ μm grating: (a) Centralized, (b) non-centralized; photon/s plot along: (c) x-axis, (d) y-axis.

the test structures is labeled. The test structures are split into two components: $r = 15$, 20, and 30 μm; and $r = 40$, 50, and 60 μm, as shown in Fig. 5(b). A typical SiN-based grating test structure is shown in Fig. 5(c), where an input grating is used to couple 1092 nm light into the waveguide, and split into multiple channels with multi-mode interferometer (MMI) to respective gratings. As 1092 nm is near to the visible range of 400–700 nm, the beams are visible under CCD camera, as shown in Fig. 5(d).

The test structure shown in Fig. 5 can be further elaborate from the GDS designs illustrated in Fig. 6(a). As shown in Fig. 6(a), An optimized input grating with 0.8 μm pitch and 0.5 duty cycle is used as the input grating coupler, where the input fiber is aligned at 13° from the z-axis. The angle between the fiber and the sample chip, $\theta = 13°$ is computed using the following equation:

$$\Lambda = \frac{m\lambda}{N - n_1 sin\theta} \tag{1}$$

where Λ, m. λ, N, and n_1 are the grating pitch, mode, wavelength, effective index of the grating, and index of the fiber, respectively. As compared to our previous study on the optimization of SOI grating under 1630 nm wavelength [8], the wavelength, λ, used in this study is lower (1092 nm). At the same time, the effective indexes, N values, of both studies are different. The N value of SOI grating under 1630 nm wavelength is ~2.687; while the N value of SiN grating under 1092 nm used in this study is ~1.758. Thus, the pitch and duty cycle used in both studies are different, where the pitch and duty cycle used in SOI grating under 1630 nm wavelength are 0.65 μm and 0.63, while the pitch and duty cycle used SiN grating under 1092 nm are 0.8 μm and 0.5. Apart from (1), there are more parameters to be considered in designing a grating, including SOI/SiN layer thickness, etch depth, duty cycle, which are not considered by (1). Thus, the ultimate design parameters employed in this study are optimized using FDTD techniques.

During a typical measurement, the fiber is aligned onto the sample chip to couple 1092 nm light into the test structure via the input grating. The coupled light is then propagated through waveguides of 10 μm and then split into separated gratings via optimized MMI. The light is then coupled out from gratings with various r values and reference grating into the beam profiler through the objective lens. Once the beam profiles appeared on the beam profiler, the distance between the profiler and the sample is manually adjusted to obtain the sharpest-possible beam profiles. A snippet of the test system is shown in Fig. 6(b). The reference gratings shown in Fig. 6 is the identical, optimized grating same as the input grating. The reference grating serves two purposes. First, it serves as a reference point to accurately locate the gratings with respectively r values. As shown in Fig. 6(c) and (d), the image of the grating is not visible under the beam profiler. By identifying the beam coupled out from the ref. grating, we can easily identify which beam belongs to $r =$ 15, 20 and 30 μm. Second, the reference grating can be used to normalize the photon count per second (photon/s) captured by the beam profiler. Since $r = 15$, 20, 30 μm and $r = 40$, 50, 60 μm are located and different test structures, the fiber-to-chip alignment was carried out such that the maximum photon/s from the reference grating from both gratings reaches 3800~3900 photon/s with variation of <5%.

IV. Results and Discussion

Fig. 6(c) and (d) shows the beam profiles of light coupled out from gratings with $r = 15$–60 μm under ×20 magnification. The separation distance between each beam is measured as ~105 μm, similar to the GDS design shown in Fig. 6(a) The coupling loss of the input and reference grating is measured as 12.53 dB per grating. On top of that, the propagation loss of the 1×0.4 μm SiN waveguide is measured as 3 dB/cm. As Fig. 6(c) and (d) is plotted from the data points of DataFrames in Python, to investigate the beam waists and FWHM of beams coupled out from respective gratings, the DataFrames are sliced as presented in Fig. 7(a).

Typically, the FWHM and beam waist at $1/e^2$ can be determined by finding the widest part of the beam along x-axis and y-axis (Fig. 7(a)), plot the photon/s against the respective x- and y-position, and determine the respective FWHM and beam waist at $1/e^2$ using the scipy package in Python, as described in ref. [16]. Similar plots of photon/s along x- and y-axis with respective peaks, FWHM, and beam waist are shown in Fig. 7(c) and (d). However, the output beam has asymmetrical shape,

possibly attributing geometrical deviation during the fabrication process. Thus, it is challenging to use visual judgement to determine the widest widths of the beam. As a result, the point where the beam has the highest photon/s value may not have the widest FWHM and beam waist. As this study mainly focuses on the development of grating structure for the optical addressing of trapped ion (Fig. 1), our main concern is to "hit" the trapped ion with the buried grating. Thus, the main figure-of-merit is the FWHM and beam waist of the light from the grating.

Thus, our aim is to develop an automated technique which locates the widest beam waist and FWHM with high photon/s along x- and y-axis, regardless of the irregularity of the beam profile and the non-centralized positioning of the beam, as shown in Fig. 7(b). To achieve this, every column and row of the beam profile's DataFrame is plotted. Peaks, FWHM and beam waist of each row and column is computed to find the widest FWHM and beam waist among the plotted rows and columns, similar to the method described in ref. [16]. However, as the experimental data of the beam profile can be uneven and asymmetrical, merely finding the widest beam profile may result in undesired plot. For instance, the white dotted line shown in Fig. 7(a) has the widest beam waist as computed, which is undesirable in our application.

The full Python code to find the widest-beam waist plots along x-axis and y-axis is shown in ref. [18]. In the case of y-axis, each column of the DataFrame is plotted and their respective peaks, beam waist, and FWHM is computed using scipy package in Python. Then, the columns will be filtered into a new DataFrame under two conditions. For each column (or each plot along y-axis), the column will be selected if: (1) the second highest peak of the column is 'n' times smaller than the highest peak of the column; (2) the highest peak of the column is no less than 60% of the maximum value in the DataFrame. Within the new DataFrame, the column with the largest beam waist will be identifies where the corresponding beam waist and FWHM will be computed. The same technique can be used for rows in the DataFrame, which corresponds to the plots along x-axis. As a result, the Python code can accurately identify the widest part of the beam along x- and y-axis, regardless of the asymmetrical shape, irregular distribution of photon/s, and non-centralized positioning. (ref. Fig. 7(a) and (b)).

Fig. 8(a) and (b) show the photon/s plots along x- and y-axis for gratings with r values ranging from 15 to 60 μm. These plots are created as a result of columns and rows selection described earlier, where columns and rows with largest beam waists are selected for these plots. From Fig. 8(a), more than one peak is observed along x-axis due to the presence of multiple modes of light from the grating structure [19]. This aligns well the simulation results presented in Fig. 2. However, compared to Fig. 2, less beam spots are observed in the beam profiles presented in Fig. 7 and the photon/s plots in Fig. 8. This can be due to the sensitivity limitations of the beam profiler. As higher order modes have weaker intensity [20], [21], higher order beams shown in Fig. 2 may not be captured by the beam profiler. At the same time, it can be observed that the beam waist along x-axis does not show any significant changes with increasing r values, despite varying photon/s intensity. This

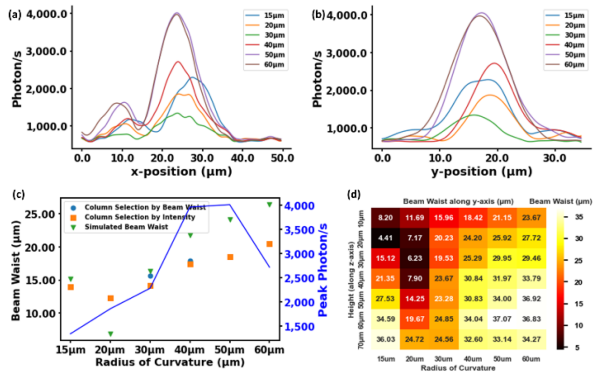

Fig. 8. Photon/s plot along (a) x-axis, (b) y-axis; (c) simulated and experimentally-obtained peak widths along y-axis, (d) heatmap of simulated peak-widths along y-axis.

agrees well with the simulated outcomes shown in Fig. 3 and ref. [8]. On the other hand, the beam waist along y-axis changes gradually across r values ranging from 15 to 60 μm.

The beam waist along y-axis (under $1/e^2$ height) obtained using the Python code illustrated in ref. [18] is shown in Fig. 8(c). As a comparison, an alternative computational technique is used to plot the beam waist along y-axis. Similar to the technique used in obtaining Fig. 3 plots from the E-field distribution shown in Fig. 2, the beam waist is determined by searching the maximum value of the whole DataFrame used for photon/s plotting (Fig. 7), where the associated column of the maximum value is plotted as the E-field along y-axis. In Fig. 8(c), the beam waists obtained using Python code described in ref. [18] is labeled as "Selection by Largest Beam waist"; whereas the beam waists obtained by the above-mentioned alternative computational technique is labeled as "Selection by Highest Photon/s". From Fig. 8(c), both techniques result in similar beam waists. This shows that the beams coupled out from the gratings exhibit Gaussian intensity profile [22], where the point with highest E-field intensity is associated with the widest beam waist along x- and y-axis.

From Fig. 8(c), the measured beam waist along y-axis focused from 13.96 to 12.3 μm as the r value increases from 15 to 20 μm. As the r value increases further to 60 μm, the beam waist increases from 12.3 to 20.51 μm. Overall, the changes in beam waist with increasing r value obtained from the experimental measurement exhibit similar characteristics as the simulated beam waist. Similar to the experimentally-measured widths, the simulated beam waist along y-axis focused as the r value increases from 15 to 20 μm. As the r value increase further to 60 μm, the beam waist increases with the radius of curvature. Similar trends are observed for heights above 20 μm. However, the simulated beam waist shown in Fig. 8(c) exhibits a significant dip when $r = 20$ μm. This is also reflected in Fig. 8(d), where the beam waist at $r = 20$ μm is significantly narrower across all heights. In contrast, the significant reduction in beam waist is not observed in the experimentally-measured beam waist, where the beam waist slightly reduced from 12.96 to 12.3 μm as r value increases from 15 to 20 μm. The simulation-experiment deviation can be attributed to the fabrication inaccuracy. From Fig. 8(c) and (d), $r = 20$ μm exhibits a distinctive reduction

in beam waist compared to $r = 15$ μm and $r = 30$ μm. In other words, high level of fabrication accuracy is needed to achieve exact r value of 20 μm, where slight structural inaccuracy may alter the r value. Fabricating curved structures with high structural accuracy is generally challenging, where slight deviations in lithography and dry etching processes may result in structural inaccuracy, which causes the output beams to have higher-than-expected beam waists [23], [24]. Nevertheless, both simulation and experimental outcomes show that the beam waist along y-axis generally increasing as the r value increases from 15 to 60 μm, with an exception where the beam waist reduces when the r value increases from 15 to 20 μm. The narrowest beam waist obtained is 12.3 μm from $r = 20$ μm grating, while the widest beam waist is 20.51 μm obtained from $r = 60$ μm. At the same time, gratings with $r = 40$ and 50 μm show the highest peak photon/s while grating with $r = 15$ μm has the lowest photon/s.

In the context of optical addressing of trapped ion, Sr^+ ion arrays are typically trapped with inter-ion distance of 10$\sim$15 μm depending on the applied pseudopotential, as reported in previous study of our research group [25], [26], [27]. For the optical addressing of single Sr^+ ion, grating with $r = 20$ μm can be used with narrower beam waist of 12.3 μm. If optical addressing of two Sr^+ ions is needed, $r = 60$ μm grating can be employed. On top of that, the trapping height of trapped Sr^+ can be 20, 40, or 80 μm above the ion trap electrode surface (Fig. 1(a)), depending on the geometrical design of the ion trap [28]. From the simulated E-field distribution at 10–70 μm, the output angle where the light coupled out from the grating (pitch = 1.2 μm) is computed as 47.03° from the z-axis illustrated in Fig. 1(b), which is similar to the output angle, 49.5°, calculated using (1). Combining the simulation and experimental results on the beam waists, beam propagation angle, and beam intensity (peak photon/s) across r values from 15 to 60 μm, the results obtained from this study provide an insightful view on the optical properties of beams coupled out from gratings with varied radius of curvature (r) values. From the obtained optical properties, a versatile solution for the optical addressing of trapped ion can be developed, which can further enhance the feasibility of electro-optical integration of ion trap for quantum devices applications.

The Python-based data analysis techniques introduced in this study provide a standardize, automated solution for multiple beam profiles. Fundamentally, the pixels of the obtained beam profiles are imported as DataFrames, where desired width along x- and y-axis can be obtained by two ways: (1) identifying the maximum value in the DataFrame and plot the corresponding rows and columns (which associated with the photon/s along x- and y-axis) to find the respective beam waists, or (2) directly identifying the maximum beam waists across all rows and columns, where filtering condition is needed. After identifying the rows and columns using either of the abovementioned conditions, the photon/s can be plotted along x- or y-position. However, it is possible that multiple peaks can occur in the same plot. Thus, widest beam waist along the plot is selected and recorded as the beam waist of light emitted from the corresponding grating structure. The details of the complete codes can be found in ref. [16], [18], as mentioned earlier.

Apart from the Python-based data analysis techniques developed in this study, the key parameters, including beam waist, FWHM and peak coordinates can also be computed by using alternative methods. For instance, the beam waists and peaks were computed with manual computational techniques in our previous study [8]. However, the manual computational techniques can be time-consuming for large datasets. Apart from Python, studies have also been reported in analyzing and processing photonics data using other types of codes, including Matlab [29], [30] and Structured Query Language (SQL) [31]. Readers can leverage the state-of-the-art artificial intelligence (AI) tools (e.g., ChatGPT) to translate the Python codes developed in this study to their most familiar coding languages (Matlab or SQL) to expand the scope of this work.

Moving forward, the propagation of beams along z-axis should be further investigated by taking a beam profile data with varying lens-to-profiler distances (ref. Fig. 6(b)), with a small step size of 1 μm. This may result in 50–100 sets of beam profiles for each grating sample. Traditional techniques such as manual computation and analysis of beam profiles can be time-consuming to analyze such amount of beam profile data. Thus, the developed Python-based techniques can be convenient in performing standardized, rapid analysis.

V. Conclusion

Grating structures with 15 to 60 μm radius of curvatures (r) is developed for the optical addressing of Sr^+ trapped ion using 1092 nm laser. The beam waists along x- and y-axis are investigated. It observed that the beam waist along x-axis has no direct correlation with varied r values. From the measured beam profiles, grating with $r = 20$ μm has the narrowest beam waist of 12.3 μm; while $r = 60$ μm has the widest beam waist of 20.51 μm. From both simulation and experimental results, it can be observed that the beam waist reduces as the r value increases from 15 to 20 μm, where the beam waist then increases as the r value increases from 20 to 60 μm. On top of that, automated Python-based data analysis techniques are developed to locate the widest part along x- and y-axis of the beam profile, regardless of its irregularity, non-centralized positioning, and asymmetrical shape. Nevertheless, as the beam profiles are measured using manually-focused beam profilers, experimental measurements on the beam profiles at various heights (10–70 μm) pose a challenge. To resolve this issue, usage of automated, motorized z-positioners can be used to measure the beam profiles at with height variation step size of > 1 μm. This can be an extension to this study to provide further insights on the influence of r values on the optical properties of beam coupled out from grating structures. Overall, the optical characteristics obtained from this study provide technical insights on the optical addressing of trapped ions using grating structure. On top of that, the developed Python-based beam profile analysis technique provide an automated, standardize method in determining key parameters of beam widths, which prepares a convenient pathway to analyze mass amount of beam profile data.

ACKNOWLEDGMENT

This work was supported by ANR-NRF Joint Grant Call under Grant NRF2020-NRF-ANR073 HIT. The authors would like to thank Advance Micro Foundry (AMF) for their support in multi-project wafer (MPW) fabrication.

REFERENCES

[1] J. Stuart et al., "Chip-integrated voltage sources for control of trapped ions," *Phys. Rev. Appl.*, vol. 11, no. 2, 2019, Art. no. 024010, doi: 10.1103/PhysRevApplied.11.024010.

[2] K. R. Brown, J. Kim, and C. Monroe, "Co-designing a scalable quantum computer with trapped atomic ions," *NPJ Quantum Inf.*, vol. 2, no. 1, pp. 1–10, 2016, doi: 10.1038/npjqi.2016.34.

[3] K. K. Mehta, "Integrated optical quantum manipulation and measurement of trapped ions," Ph.D. dissertation, Massachusetts Inst. Technol., Cambridge, MA, USA, 2017.

[4] R. J. Niffenegger et al., "Integrated multi-wavelength control of an ion qubit," *Nature*, vol. 586, no. 7830, pp. 538–542, 2020, doi: 10.1038/s41586-020-2811-x.

[5] K. K. Mehta, C. Zhang, M. Malinowski, T. L. Nguyen, M. Stadler, and J. P. Home, "Integrated optical multi-ion quantum logic," *Nature*, vol. 586, no. 7830, pp. 533–537, 2020, doi 10.1038/s41586-020-2823-6.

[6] H. McGuinness et al., "Integrated photonics for trapped ion quantum information experiments at Sandia National Laboratories," *Proc. SPIE*, vol. 12206, 2022, Art. no. 1220604, doi: 10.1117/12.2636695.

[7] S. Li et al., "Deterministic design of focusing apodized subwavelength grating coupler based on weak form and transformation optics," *Opt. Exp.*, vol. 28, no. 23, 2020, Art. no. 35395, doi: 10.1364/oe.409981.

[8] Y. D. Lim, H. Y. Li, P. Zhao, J. Tao, L. Guidoni, and C. S. Tan, "Design and fabrication of grating couplers for the optical addressing of trapped ions," *IEEE Photon. J.*, vol. 13, no. 4, Aug. 2021, Art. no. 2200306, doi: 10.1109/jphot.2021.3094646.

[9] T. Hu et al., "Silicon photonic platforms for mid-infrared applications," *Photon. Res.*, vol. 5, no. 5, pp. 417–430, 2017, doi: 10.1364/prj.5.000417.

[10] P. Muñoz, "Photonic integration in the palm of your hand: Generic technology and multi-project wafers, technical roadblocks, challenges and evolution," in *Proc. Opt. Fiber Commun. Conf. Exhib.*, 2017, pp. 1–3.

[11] P. Zhao et al., "TSV-integrated surface electrode ion trap for scalable quantum information processing," *Appl. Phys. Lett.*, vol. 118, 2021, Art. no. 124003, doi: 10.1063/5.0042531.

[12] K. K. Mehta and R. J. Ram, "Precise and diffraction-limited waveguide-to-free-space focusing gratings," *Sci. Rep.*, vol. 7, no. 1, pp. 1–8, 2017, doi: 10.1038/s41598-017-02169-2.

[13] K. A. Bates, L. Li, R. L. Roncone, and J. J. Burke, "Grating couplers in planar waveguides," *Appl. Opt.*, vol. 32, no. 12, pp. 2112–2116, 1993.

[14] T. Sharma et al., "Coupling performance enhancement using SOI grating coupler design," *Opt. Commun.*, vol. 427, pp. 452–456, 2018, doi: 10.1016/j.optcom.2018.06.012.

[15] C.-S. Im, B. Bhandari, K.-P. Lee, S.-M. Kim, M.-C. Oh, and S.-S. Lee, "Silicon nitride optical phased array based on a grating antenna enabling wavelength-tuned beam steering," *Opt. Exp.*, vol. 28, no. 3, 2020, Art. no. 3270, doi: 10.1364/oe.383304.

[16] Y. D. Lim, "Peak width, peak position, and FWHM of simulated beam profile along x-axis and y-axis," *github.com*. Accessed: Feb. 23, 2023. [Online]. Available: https://github.com/yd145763/different_radius_publication_data_code/blob/main/plot%20everything.py

[17] L. Cheng, Y. Luo, Q. Qian, S. Wu, and H. Chen, "Compact beam shaping design based on polarization plane multiplexing of semiconductor lasers," *Appl. Opt.*, vol. 61, no. 30, 2022, Art. no. 8994, doi: 10.1364/ao.467643.

[18] Y. D. Lim, "Determining the columns and rows with the widest beam width in the beam profile's dataframe," *github.com*. Accessed: Mar. 1, 2023. [Online]. Available: https://github.com/yd145763/different_radius_publication_data_code/blob/main/widest%20column%20and%20rows%20with%20filtering.py

[19] C. Alonso-Ramos et al., "Single-etch grating coupler for micrometric silicon rib waveguides," *Opt. Lett.*, vol. 36, no. 14, pp. 2647–2649, 2011, doi: 10.1364/OL.36.002647.

[20] B. Wohlfeil, G. Rademacher, C. Stamatiadis, K. Voigt, L. Zimmermann, and K. Petermann, "A two-dimensional fiber grating coupler on SOI for mode division multiplexing," *IEEE Photon. Technol. Lett.*, vol. 28, no. 11, pp. 1241–1244, Jun. 2016, doi: 10.1109/LPT.2016.2514712.

[21] I. Demirtzioglou et al., "Apodized silicon photonic grating couplers for mode-order conversion," *Photon. Res.*, vol. 7, no. 9, 2019, Art. no. 1036, doi: 10.1364/prj.7.001036.

[22] S. Kim et al., "Photonic waveguide to free-space Gaussian beam extreme mode converter," *Light Sci. Appl.*, vol. 7, no. 1, 2018, Art. no. 72, doi: 10.1038/s41377-018-0073-2.

[23] T. K. Kim et al., "Curved structure of si by improving etching direction controllability in magnetically guided metal-assisted chemical etching," *Micromachines*, vol. 11, no. 8, 2020, Art. no. 744, doi: 10.3390/MI11080744.

[24] L. Li and A. Y. Yi, "Microfabrication on a curved surface using 3D microlens array projection," *J. Micromechanics Microengineering*, vol. 19, no. 10, 2009, Art. no. 105010, doi: 10.1088/0960-1317/19/10/105010.

[25] P. Zhao et al., "Glass substrate interposer for TSV-integrated surface electrode ion trap," in *Proc. IEEE 22nd Electron. Packag. Technol. Conf.*, 2020, pp. 262–265, doi: 10.1109/EPTC50525.2020.9315003.

[26] P. Zhao et al., "Performance comparison of high resistivity silicon, silicon with grounding plane and glass as substrate of ion trap for quantum information processing," in *Proc. IEEE 8th Electron. Syst.-Integration Technol. Conf.*, 2020, pp. 1–5, doi: 10.1109/ESTC48849.2020.9229689.

[27] P. Zhao, J. Tao, H. Y. Li, Y. D. Lim, L. Guidoni, and C. S. Tan, "Design, fabrication and characterization of surface electrode ion trap integrated with TSV," in *Proc. IEEE 21st Electron. Packag. Technol. Conf.*, 2019, pp. 13–17, doi: 10.1109/EPTC47984.2019.9026716.

[28] A. A. A. Apriyana et al., "Design and development of single-qubit ion trap on glass and si substrates with RF analysis and performance benchmarking," *IEEE Trans. Compon., Packag. Manuf. Technol.*, vol. 10, no. 7, pp. 1221–1231, Jul. 2020, doi: 10.1109/TCPMT.2020.2995388.

[29] M. Engineering, N. K. All, K. Lyngby, and D. Nanophoton, "Compact 200 line MATLAB code for inverse design in photonics by topology optimization : Tutorial," *J. Opt. Soc. Amer. B*, vol. 38, no. 2, pp. 510–520, 2021.

[30] J. I. J. Iang et al., "MetaNet : A new paradigm for data sharing in photonics research," *Opt. Exp.*, vol. 28, no. 9, pp. 13670–13681, 2020.

[31] H. J. Kim, J. W. Sohn, N. Hong, C. Williams, and W. Humphreys, "PCM-net: A refractive index database of chalcogenide phase change materials for tunable nanophotonic device modelling," *J. Phys.: Photon.*, vol. 3, no. 2, 2021, Art. no. 024008, doi: 10.1088/2515-7647/abeb55.